An integrated framework for finite-element modeling of mitral valve biomechanics from medical images: Application to MitralClip intervention planning

Tommaso Mansi [a,*], Ingmar Voigt [a,b], Bogdan Georgescu [a], Xudong Zheng [a], Etienne Assoumou Mengue [a], Michael Hackl [c], Razvan I. Ionasec [a], Thilo Noack [d], Joerg Seeburger [d], Dorin Comaniciu [a]

[a] Siemens Corporation, Corporate Research and Technology, Image Analytics and Informatics, Princeton, NJ, USA
[b] Friedrich-Alexander-University, Pattern Recognition Lab, Erlangen, Germany
[c] Friedrich-Alexander-University, Medizinische Fakultät, Erlangen, Germany
[d] Heart Centre Leipzig, Department of Cardiac Surgery, Leipzig, Germany

ARTICLE INFO

ABSTRACT

Treatment of mitral valve (MV) diseases requires comprehensive clinical evaluation and therapy personalization to optimize outcomes. Finite-element models (FEMs) of MV physiology have been proposed to study the biomechanical impact of MV repair, but their translation into the clinics remains challenging. As a step towards this goal, we present an integrated framework for finite-element modeling of the MV closure based on patient-specific anatomies and boundary conditions. Starting from temporal medical images, we estimate a comprehensive model of the MV apparatus dynamics, including papillary tips, using a machine-learning approach. A detailed model of the open MV at end-diastole is then computed, which is finally closed according to a FEM of MV biomechanics. The motion of the mitral annulus and papillary tips are constrained from the image data for increased accuracy. A sensitivity analysis of our system shows that chordae rest length and boundary conditions have a significant influence upon the simulation results. We quantitatively test the generalization of our framework on 25 consecutive patients. Comparisons between the simulated closed valve and ground truth show encouraging results (average point-to-mesh distance: 1.49 ± 0.62 mm) but also the need for personalization of tissue properties, as illustrated in three patients. Finally, the predictive power of our model is tested on one patient who underwent MitralClip by comparing the simulated intervention with the real outcome in terms of MV closure, yielding promising prediction. By providing an integrated way to perform MV simulation, our framework may constitute a surrogate tool for model validation and therapy planning.

© 2012 Elsevier B.V. All rights reserved.

1. Introduction

1.1. Clinical rationale: preoperative planning of mitral valve repair

The mitral valve (MV), located between the left atrium (LA) and the left ventricle (LV), controls the blood flow from the LA towards the LV. The MV is a complex cardiac structure comprising two leaflets, the mitral annulus and chordae tendineae. The leaflets are attached to the left heart through the fibrous mitral annulus. The other extremity, called free edge, is tethered to the papillary muscles through the chordae tendineae (Fig. 1). During diastole, the leaflets open as the blood enters the LV. When the myocardium starts to contract, the leaflets close to prevent the blood from going back to the atrium. The chordae tendineae tighten to ensure perfect closure.

Mitral valve disease is one of the most common heart valve diseases (Iung and Vahanian, 2011), with a prevalence sharply increasing with age (from 0.5% to 9.3% between 18 and ⩾75 year of age in the US (Roger et al., 2011)). Defects in leaflet morphology, chordae structure or ventricular asynchrony can result in incorrect MV closure. In this situation, the blood flows back towards the LA during systole, the so-called mitral regurgitation, thus decreasing cardiac efficiency. In severe cases, surgical intervention may be necessary to repair, or even replace the incompetent valve. The edge-to-edge technique, which consists in suturing the two mitral leaflets at the regurgitant hole, has demonstrated good clinical outcomes in patients with severe mitral insufficiency due to leaflet prolapse or calcified annulus (Maisano et al., 1998). Recently, a percutaneous device, called MitralClip, has been designed to attach the two leaflets through a catheter (Herrmann and Feldman, 2006). A careful preoperative planning is necessary to select patients and to determine the clipping sites. Strict guidelines have been defined (Feldman et al., 2009) but current selection criteria still lack predictive power with respect to complications and effectiveness of

---
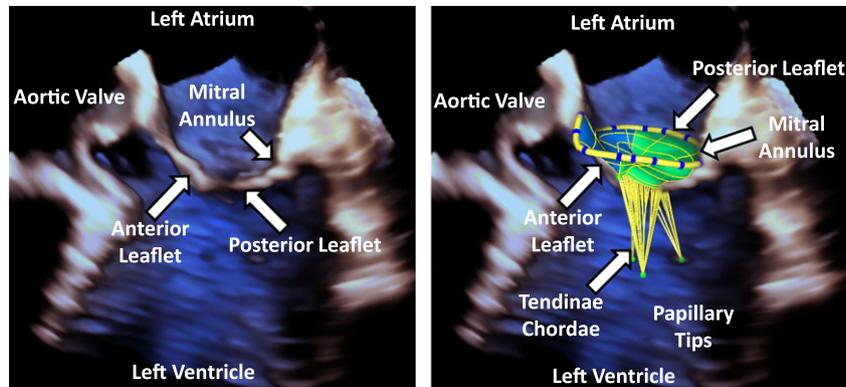
Fig. 1. 3D+t transesophageal (TEE) ultrasound image of the mitral valve.

the therapy in specific patients. It is not uncommon to perform several attempts during intervention and, in some cases, decide to place two clips (≈30% of the patients) or even to abort the procedure due to complications (≈10% of the patients) (Feldman et al., 2009). Thus, there is a need for an efficient and predictive framework that can assist the clinicians in planning the MitralClip procedure and guide them during intervention.

1.2. Technical background: computational models of the mitral valve

1.2.1. Geometrical models of MV anatomy

Comprehensive assessment of MV physiology requires detailed modeling of patient MV anatomy and dynamics from images. However, the complexity of MV anatomy and its fast dynamics make its accurate delineation from medical images difficult. Ultrasound images, and 3D+t transesophageal (TEE) in particular, are the images of choice to evaluate MV function in patients. They not only show the dynamics of the structure but also enable clinicians to compute diagnostic parameters through tedious and time-consuming delineation, with little computational assistance (Chandra et al., 2011; Jassar et al., 2011).

More automatic methods have been proposed to make MV assessment more efficient. Burlina et al. (2010) proposed an interactive algorithm based on thin-tissue detection and level-set deformable models to identify the MV and the LV endocardium in 3D TEE images. Detailed geometrical models were obtained, enabling the authors to perform patient-specific MV simulations. However, several user interactions were still necessary to guide the algorithm and no automation was provided to estimate MV anatomy throughout the cardiac cycle consistently as the method deals with frames individually. Schneider et al. proposed a complex pipeline to automatically delineate the MV from 3D+t TEE images, obtaining results with promising accuracy. The method relied on mitral annulus detection and tracking (Schneider et al., 2011b), leaflet segmentation of the open valve (Schneider et al., 2011a) and leaflet tracking using a deformable model that handled contacts and chordae stresses (Schneider et al., 2011d). Temporal resampling of 3D+t TEE images acquired on multiple heartbeats was proposed to improve temporal consistency (Schneider et al., 2011c). However, it is not clear how the authors' approach generalizes on large populations, with a wider spectrum of MV diseases, because of the numerous parameters to set.

In (Ionasec et al., 2010), we provided a fast and accurate method based on machine learning to detect the MV on 3D+t TEE or CT images. The method has been recently extended to all heart valves (Grbić et al., 2010) and papillary tips (Voigt et al., 2011b). Biomechanical constraints have also been added to improve the robustness of MV tracking (Voigt et al., 2011a). The algorithm has been validated on hundreds of patients with various heart valve diseases, showing very good robustness and accuracy.

1.2.2. Biomechanical models of MV physiology

Quantifying MV function might not be sufficient to plan the optimal treatment for a specific patient. Mechanical insights are necessary to predict how pathological MV dynamics will be modified after intervention. Furthermore, a comprehensive understanding of MV physiology is crucial in order to design long-term treatments that do not alter normal LV function. To address these questions, computational models of MV physiology have been proposed. Since the pioneering work of Kunzelman et al. (1993), several models have been proposed and new insights on MV function have been obtained. Two categories of computational MV models can be distinguished: structural models and fluid–structure interaction (FSI) models.

1.2.2.1. Structural models. Structural models aim to simulate the biomechanics of MV apparatus without directly considering the blood that flows across it. The standard approach is to use finite-element models (FEM) to solve the dynamics equation of MV leaflets, under chordae tension, surface pressure and boundary conditions (Kunzelman et al., 1993). Chordae were identified as non-linear tensile tissues very early (Kunzelman and Cochran, 1990). Biaxial stress-stretch experiments revealed that leaflets are non-linear tissues, owing to crimped collagen fibers that unfold when the leaflet are under stress, and anisotropic, as these fibers are mostly oriented parallel to the mitral annulus (May-Newman and Yin, 1995; Grashow et al., 2006; Sacks et al., 2009). Thus, although some studies relied on anisotropic linear elasticity (Kunzelman et al., 1993; Schievano et al., 2009; Krishnamurthy et al., 2009), leaflets biomechanics are mostly modeled using hyperelasticity theory (May-Newman and Yin, 1998; Prot et al., 2007). These studies enabled to analyze leaflet stress distribution during valve closure (Prot et al., 2007; Votta et al., 2008; Stevanella et al., 2009) and to quantify the effects of material properties on valve closure (Prot et al., 2010). They also highlighted the key role of MV annulus motion and papillary tips position for optimal valve closure (Stevanella et al., 2009). Considered as passive tissues until recently, leaflets may actually be active as revealed by recent studies (Krishnamurthy et al., 2009; Stevanella et al., 2011a), responding to atrial contraction. Computational models simulating this property (Skallerud et al., 2011; Swanson et al., 2011) suggested that MV shape at systole may be driven by the systolic stiffening of the leaflets.

Alternatives to FEM that require less computational power have been investigated for surgery training and therapy planning. In (Hammer et al., 2011), the authors simulated MV closure using

an anisotropic mass-spring model whose stiffness is fitted to a typical leaflet stress–strain energy. The authors successfully tested their approach on *ex vivo* pig data. Burlina et al. (2010) developed a stationary analysis framework for MV closure simulation based on shape-finding finite elements. Given a triangulated mesh, the algorithm finds the equilibrium position of its vertices by minimising a total energy that comprises external forces, contact forces, tethering forces and linear elastic energy. Sprouse et al. (2011) extended this approach to hyperelastic materials to estimate leaflet stresses. The approach was applied on two *in vivo* cases, resulting in promising prediction errors of ≈3 mm although MV annulus was deformed based on global geometrical parameters.

1.2.2.2. Fluid-structure interaction models. While structural models focus on MV biomechanics, FSI models aim to study the interactions between the MV and the blood flow by coupling FEM MV models with computational fluid dynamics (CFD) of blood flow (Einstein et al., 2010). Common approaches rely on Lagrangian frameworks (Kunzelman et al., 2007; Lau et al., 2010) or immersed boundaries methods (Watton et al., 2008). While FSI models are necessary for comprehensive analysis of MV physiology, they are significantly more complex to solve. Additionally, blood flow boundary conditions are required, which may be difficult to measure from standard clinical data. The standard approach is to immerse the MV into an idealized fluid domain (tubes (Watton et al., 2008), boxes (Einstein et al., 2010) or idealized ventricular geometries (Lau et al., 2010)), which may not reflect the actual condition of the patient. Recently, patient-specific LV geometry and dynamics from TEE ultrasound data have been used as boundary conditions to CFD solvers (Sprouse et al., 2009; Voigt et al., 2011b). However, fluid-to-solid interactions were not considered in these studies.

1.2.3. Computational analysis of MV repair

As MV modeling reaches maturity, researchers are beginning to investigate the effects of therapies on MV function. Mitral annuloplasty was simulated on a patient-specific anatomy (Votta et al., 2007; Stevanella et al., 2011b), showing that FEM models can be used to determine ring size. Reported simulations were not compared with actual outcomes. Schievano et al. (2009) investigated two different techniques for percutaneous valve dilatation using a linear elastic model (Kunzelman et al., 1993) and idealized geometries. Structural changes due to edge-to-edge repair were also simulated (Votta et al., 2002; Avanzini, 2008). In (Avanzini et al., 2011), the authors concluded that MitralClip intervention yields leaflet stresses similar to those resulting after the surgical edge-to-edge procedure. Finally, FSI modeling of the edge-to-edge procedure on idealized valve geometry identified an increased fluid jet velocity due to the double orifice (Lau et al., 2011). However, all these studies could not be evaluated against clinical data on large populations due to their idealized framework or the tedious process to get patient-specific anatomical models.

1.3. Aim of the study

Translating computational models of MV physiology to clinical practice remains a tremendous challenge. One of the major difficulty is the lack of integrated and efficient framework for MV modeling based on patient data. Studies based on *in vivo* patient images are being reported but time-consuming manual delineations are still required, with no (Stevanella et al., 2011b; Conti et al., 2010) or partial automation (Votta et al., 2008; Burlina et al., 2010). Because of the user interactions, validation is still limited to few subjects (usually ⩽5). Therefore, current approaches can hardly scale up and may yield inconsistent results due to user variability.

As a first step towards patient-specific MV FEM, we propose in this manuscript an integrated framework that combines efficient machine-learning methods with a biomechanical model of the valve apparatus to simulate MV function and therapies in patients. As illustrated in Fig. 2, and detailed in Section 2, our approach first estimates a comprehensive anatomical model of MV apparatus, including papillary tips, from the images. We then automatically build a detailed volumetric model comprising leaflet fibers, and simulate MV closure based on a biomechanical model. After parameter sensitivity analysis, we evaluated the generalization of our biomechanical model with respect to tissue properties, i.e. how accurately MV closure can be simulated by using patient geometry and boundary conditions but standard tissue parameters. MV closure was simulated on 25 consecutive patients and compared with ground truth, showing that good results can be achieved (mean point to mesh error: 1.49 ± 0.62 mm) but also highlighting the importance of personalizing tissue biomechanical parameters. Finally, we applied our framework to MitralClip planning by simulating the intervention on the preoperative data of one retrospective patient. Comparison with the real outcome in terms of MV closure suggested a promising prediction power.

This study extends our previous work (Mansi et al., 2011) as follows:

  i The anatomical model used to simulate MV closure is closer to experimental data reported in the literature, more especially leaflet thickness (Kunzelman et al., 2007; Conti et al., 2010).
  ii The biomechanical model is improved to consider tissue anisotropy. MV fiber orientation is modeled as in (Prot et al., 2009).
  iii A sensitivity analysis of the main biomechanical parameters is carried out to identify the parameters to adjust first when calibrating the model.
  iv The generalization of the biomechanical model with respect to tissue properties is tested on 25 cases.
  v A first personalization of chordae biomechanics is reported on three cases.

2. Methods

2.1. Estimation of mitral valve apparatus from 3D+t TEE images

In this study, MV anatomy is estimated from 3D+t TEE images. The model comprises (Fig. 3): the mitral annulus, the anterior and posterior leaflets (henceforth denoted AL and PL respectively), and the anterior and posterior papillary tips. To capture a broad spectrum of morphological variations, the model is parameterized by three coarse-to-fine components: (i) Three transformations B for global location, orientation and scale over the cardiac cycle; (ii) The trajectories of nine anatomical landmarks $L(B) = (\mathbf{l}_1 \ldots \mathbf{l}_9) \in \mathbb{R}^{3 \times 9}$ (two trigones, one posterior annulus mid-point, two commissures, two leaflet tips and two papillary tips); and (iii) a triangulated surface mesh $S_{LA}(B, L)$ to represent the left atrial (LA) surface of both AL and PL. The position of the vertices of the LA surface is constrained by the anatomical landmarks, resulting in an anatomically consistent parameterization $(\Omega, \mathbf{u}, \mathbf{v})$ that ensures intra- and inter-patient point correspondence (Ionasec et al., 2010). Ω is the vertex of the mitral annulus that is directly perpendicular to the anterior commissure, $\mathbf{u}$ ($\mathbf{v}$ *resp.*) is the curvilinear coordinate tangent (radial *resp.*) to the annulus. u_{res} and v_{res} are the resolutions along the $\mathbf{u}$- and $\mathbf{v}$- coordinates respectively.

B, $L(B)$ and $S_{LA}(L, B)$ are estimated from the images using a hierarchical discriminative learning algorithm (Fig. 4). The probability $p(B, L, S|I)$ knowing the image data I is incrementally modeled within the Marginal Space Learning (MSL) framework, based
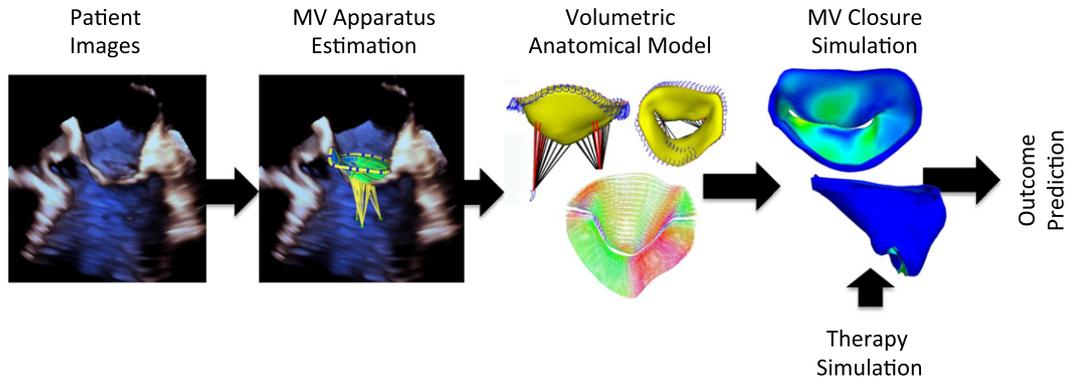
Fig. 2. The main steps of the proposed framework for MV closure simulation.
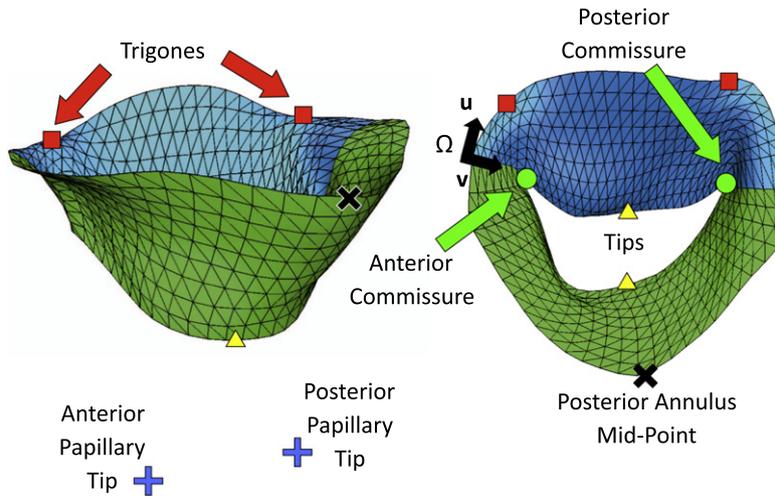
Fig. 3. Anatomical model of the MV and sub-valvular apparatus that is estimated from clinical images. Leaflets are uniquely parametrized through the curvilinear coordinates $(\Omega, \mathbf{u}, \mathbf{v})$ calculated from the detected landmarks.
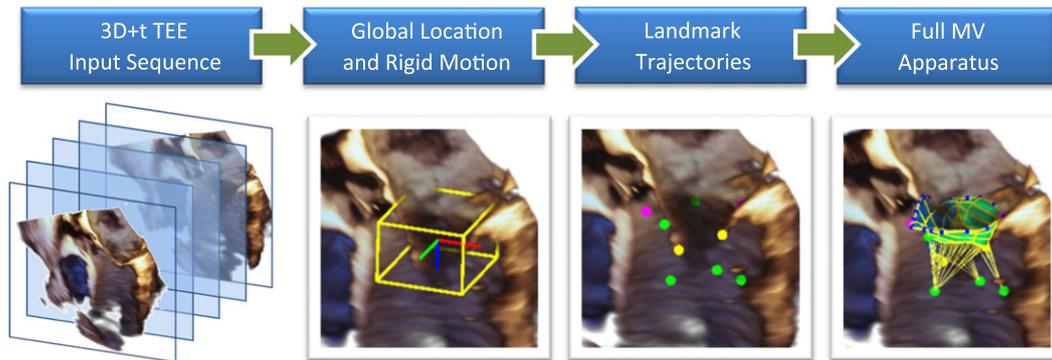
Fig. 4. The main steps of the automatic estimation pipeline. We first estimate the global position of the MV, then detect the MV landmarks inside this region of interest and finally map and deform triangulated surfaces to segment the MV leaflets.

on the Probabilistic Boosting Tree (PBT). Intuitively, given a test image, MLS framework first finds position candidates around the MV based on Haar- and steerable features. The position candidates are then successively refined by rotation and scaling candidates. This defines a region of interest inside which the position of nine landmarks is estimated using the same strategy. Next, a point-distribution model of the MV surface is mapped according to the landmarks and deformed, within the learned space of shapes, according to boundary detectors estimated through PBT. Finally, the complete MV anatomy is tracked over the car-

diac sequence using a manifold-based motion model. The reader is referred to (Zheng et al., 2008; Ionasec et al., 2010) for further details.

2.2. Volumetric anatomical model of the MV apparatus

In a second stage, we extend the surface model by (i) generating a thick, tetrahedral representation of MV leaflets, (ii) adding MV leaflet fiber orientation to capture tissue anisotropy and (iii) modeling MV chordae.

2.2.1. Tetrahedral representation of MV leaflets

MV biomechanics are computed using tetrahedral FEM (Section 2.3). The thick geometry of MV leaflets must therefore be modeled but due to the inconsistent quality of ultrasound images, accurate measurement of leaflet thickness from the images is still challenging. Instead, we compute the LV surface of the leaflets, S_{LV}, by extruding the previously S_{LA} towards the ventricle. The surfaces S_{LA} and S_{LV} are merged at the free edges and annulus to obtain the thick geometry. Leaflet thickness is directly controlled by the extrusion depth, here 1.32 mm and 1.26 mm for the AL and PL respectively, as in (Votta et al., 2008; Kunzelman et al., 2007). Tetrahedral elements are created between S_{LA} and S_{LV} by connecting the surface vertices. Thus, the number of tetrahedra is directly controlled by the parameters u_{res} and v_{res}, and point correspondence is ensured across time frames and patients. For regional personalization, each element is automatically tagged according to the leaflet it belongs to (Fig. 5, left panel).

2.2.2. MV fibers modeling

Current *in vivo* imaging technology cannot quantify the orientation of leaflet collagen fibers. Thus, their direction is modeled as in (Prot et al., 2009), following the experimental observations reported in (May-Newman and Yin, 1995). Fibers are mainly parallel to the annulus (circumferential direction). For the AL, the fibers close to the commissures gradually rotate to become perpendicular to the annulus (radial direction) (Fig. 5, right panel).

2.2.3. MV chordae modeling

Twenty-eight marginal chordae are defined, evenly attached between papillary tips and leaflet free edges (Hammer et al., 2008; Votta et al., 2008). Four basal chordae are attached to each leaflet, two for each papillary tip (Fig. 6). To avoid any bias in the evaluation, insertion points are identical across subjects owing to the point correspondence. More precisely, the insertion points of the marginal chordae are defined by $(u, v) = (ku_{res}/28, v_{res} - 1)$, where $k \in [[0 : 27]]$. Basal insertion points are defined by $(u, v) = ((2i + 1)u_{res}/8, (v_{res} - 1)/2)$ and $(u, v) = ((2i + 1)u_{res}/8 + 1, (v_{res} - 1)/2), i \in [[0 : 3]]$.

2.3. Biomechanical model of mitral valve apparatus

Valve closure is simulated by solving the dynamics system:

$$\mathbf{M\ddot{U}} + \mathbf{C\dot{U}} + \mathbf{KU} = \mathbf{F}_c + \mathbf{F}_p \tag{1}$$

U is the displacement vector of the free vertices of the MV mesh, $\dot{\mathbf{U}}$ the velocity vector and $\ddot{\mathbf{U}}$ the acceleration vector. M is the lumped mass matrix (a uniform mass density $\rho = 1.04$ g/mL is used, Table 1). K is the stiffness matrix of the internal elastic forces.

C is the damping matrix modeling the viscosity of the system. It also increases system robustness under strong collisions. In this work, C is a linear combination of stiffness and mass matrices (Rayleigh damping), $C = \alpha_M M + \alpha_K K$. Non-reported experiments identified $\alpha_M = 0.1$ s^{-1} and $\alpha_K = 0.1$ s as a good compromise between system damping and robustness. $\mathbf{F}_c$ and $\mathbf{F}_p$ are the forces developed by the chordae and heart pressure respectively.

2.3.1. Leaflet passive properties

MV leaflets are modeled as linear, transverse isotropic elastic tissues (Hammer et al., 2008; Schievano et al., 2009; Krishnamurthy et al., 2009) as we are not directly interested in leaflet stresses during the entire cardiac cycle but we rather seek to predict how well they close during systole to assess possible residual regurgitant holes after intervention. Besides, recent works based on inverse-problem methods suggested that the leaflets may behave as linear materials in the range of physiological pressures (Krishnamurthy et al., 2009). In our experiments, different tissue properties are assigned to the AL and PL. The Young moduli corresponding to the tangent elastic modulus measured at large strains are used (values from (Schievano et al., 2009) and estimated experimentally in (Kunzelman et al., 1993)) (Table 1).

2.3.2. Chordae passive properties

Chordae are modeled by piecewise tensile springs between papillary tips, modeled as spatial points, and leaflet insertion points (Fig. 6). Between an insertion point $\mathbf{v_i}$, $i \in \{\text{marginal}, \text{basal}\}$ and its corresponding papillary tip $\mathbf{p_i}$, we apply the force:

$$\mathbf{f}_c(\mathbf{v_i}, \mathbf{p_i}, t) = -k_{c,i}(\epsilon_{c,i}, t) \times (L_i(t) - L_{i,0}), \tag{2}$$

where L_i is the current elongation $\|\mathbf{v_i}(t) - \mathbf{p_i}(t)\|$, $\epsilon_{c,i}(t) = (L_i(t) - L_{i,0})/L_{i,0}$ is the strain and $L_{i,0}$ is the chordae rest length, defined as the distance between the papillary tips and the insertion points estimated at the end diastole time frame. At compression, when $\epsilon_{c,i}(t) \leqslant 0$, $k_{c,i} = 0$ g/mm^2 to model free compression. During tension, the non-linear response of the chordae (Fig. 7, left panel) is approximated using a piece-wise constant stiffness function $k_{c,i}(\epsilon_{c,i}, t)$. Spring tensile stiffnesses $k_{c,i}$ are calculated from the chordae Young moduli according to $k_{c,i} = A_{0,i}E_{c,i}/L_{0,i}$ where $A_{0,i}$ is the chordae cross-section at rest. The parameters used in this study were estimated experimentally in (Kunzelman and Cochran, 1990) and reported in Table 1.

2.3.3. External loads, boundary conditions and contacts

We simulated valve dynamics between end of diastole, defined as the last time frame when the valve is seen fully open, and the first systolic frame, defined as the first frame when the valve is seen maximally closed (fully closed if not pathological). Since pres-
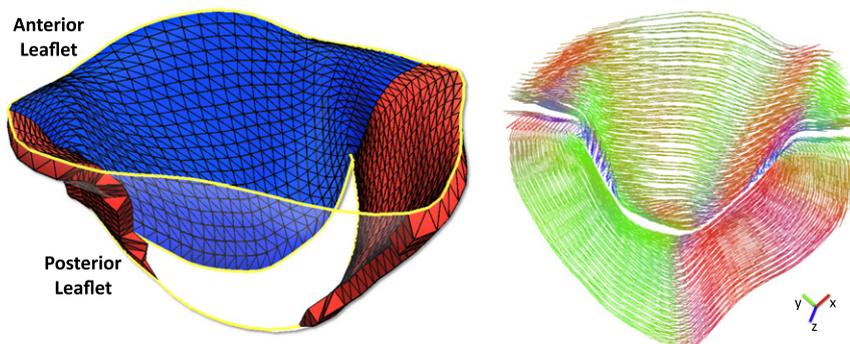
Fig. 5. *Left panel:* Tetrahedral mesh of MV leaflets. Colors encode element tag for regional personalization. *Right panel:* Computational model of MV fiber orientation. Fibers are oriented mainly parallel to the annulus. On the anterior leaflet, fibers become radial close to the commissures. Colors encode fiber direction. (For interpretation of the references to colour in this figure legend, the reader is referred to the web version of this article.)
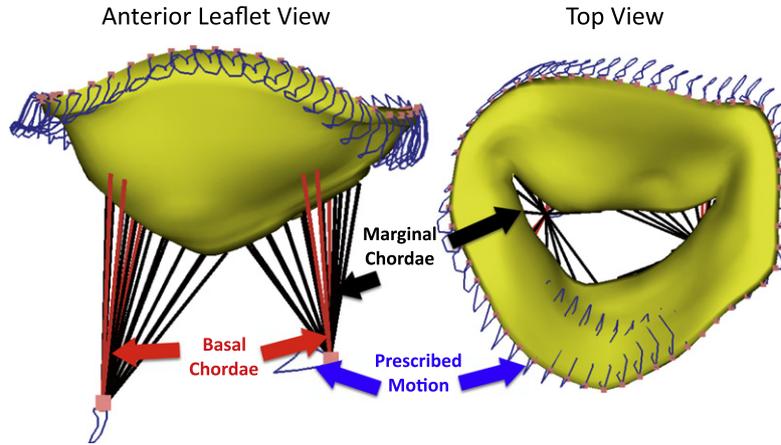
Fig. 6. Tendineae chordae and boundary conditions (Patient 25). Chordae are inserted in the leaflets at the same spatial location for all patients owing to the point correspondence. Mitral annulus and papillary tips motions are prescribed from image data.

Table 1
Parameters of the biomechanical model.

Leaflets (from Schievano et al. (2009)	
Mass density	ρ = 1.04 g/mL
Poisson ratio	v = 0.488
AL Young's modulus	$E_{AL_f} = 6.233$ MPa, $E_{AL_\perp} = 2.350$ MPa
AL shear modulus	$G_{ff\perp} = 1.369$ MPa
PL Young's modulus	$E_{PL_f} = 2.087$ MPa, $E_{PL_\perp} = 1.887$ MPa
PL shear modulus	$G_{ff\perp} = 0.694$ MPa
Marginal chordae (from Kunzelman and Cochran (1990)	
Young's modulus ($\epsilon < 2.5\%$)	$E_c = 312$ g/mm^2
Young's modulus ($\epsilon \geqslant 2.5\%$)	$E_c = 3406$ g/mm^2
Cross-section	$A_0 = 0.40$ mm^2
Basal chordae (from Kunzelman and Cochran (1990)	
Young's modulus ($\epsilon < 5\%$)	$E_c = 66$ g/mm^2
Young's modulus ($\epsilon \geqslant 5\%$)	$E_c = 2120$ g/mm^2
Cross section	$A_0 = 2.05$ mm^2
General	
Time step	dt = 0.01 s
Mesh resolution	$u_{res} = v_{res} = 30$
Number of marginal chordae	28
Number of basal chordae	4
k_{clip}	1000 g/mm

sure values were unknown for the patients, we assumed a generic profile that increases from 0 mmHg to 120 mmHg (Fig. 7, right panel), as in (Prot et al., 2009; Stevanella et al., 2011b; Hammer et al., 2011). The motions of the papillary tips and of the mitral annulus are prescribed from the automatic detection (Fig. 6). In practice the displacement and velocity of the prescribed vertices are projected at every time step of the simulation such that they correspond to the motion observed in the images. Finally, self-collisions are detected using a ray-casting approach (Hermann et al., 2008). At every time step, the distance between a leaflet vertex and the leaflets, along vertex normal, is calculated. If that distance is lower than an alarm distance $d_c = 0.6$ mm, then a spring is added between the vertex and the collision point to ensure a minimal collision distance of 0.3 mm. Tangential interaction is modeled with a friction coefficient of 0.5.

2.4. MitralClip simulation

Virtual mitral clipping is performed interactively, in real-time, on the open configuration of the preoperative anatomy. The pressures are disabled and mitral annulus and papillary tips are fixed to facilitate user interactions. The user first picks a vertex on each leaflet (Fig. 8A). A stiff spring ($k_{clip} = 1000$ g/mm) is then created between the two vertices, which makes the leaflets progressively close at the clip location (Fig. 8B) according to their internal consti-
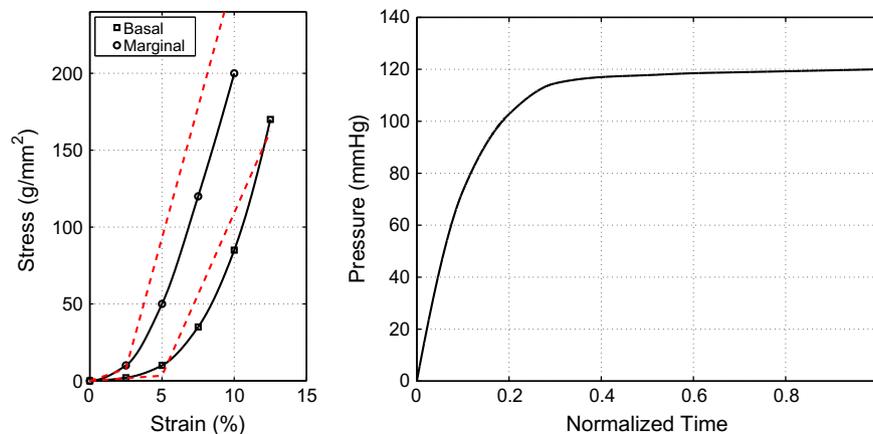
Fig. 7. *Left panel:* Stress–strain behavior of chordae. Linear approximation in dashed lines (data from Kunzelman and Cochran (1990)). *Right panel:* Pressure profile applied to the leaflets to simulate closure. The time is adjusted for each patient to match valve closure duration.
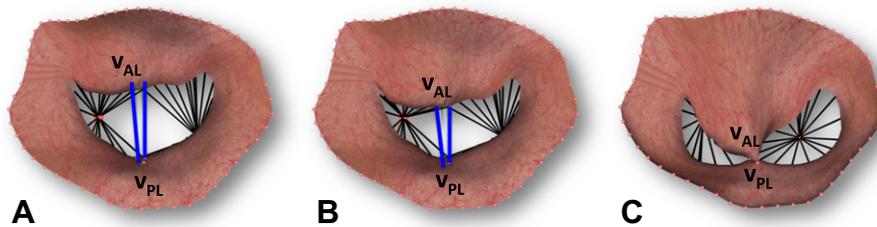
Fig. 8. Interactive simulation of MitralClip procedure. The user picks two vertices on each leaflet ($\mathbf{v}_{AL}$ and $\mathbf{v}_{PL}$) (**A**). A spring is created between the picked vertices (*blue lines*) that will progressively (**B**) stitch the leaflets together (**C**). (For interpretation of the references to colour in this figure legend, the reader is referred to the web version of this article.)

tutive law and chordae tension. The stiffness of the spring is strong enough to hold the leaflets together and model the clip (Fig. 8**C**).

Once the clip is implanted, postoperative MV closure is simulated to assess the efficacy of the intervention in terms of MV regurgitation, just after clip release. To that end, we assume the ventricle motion to be similar to the preoperative motion, as only the morphology of the leaflets changed. Preoperative boundary conditions and ventricular pressures are applied on the clipped geometry to simulate closure.

2.5. Implementation

The biomechanical model is implemented using SOFA,[1] an open-source soft-tissue intervention framework (Allard et al., 2007). Eq. (1) is solved using co-rotational linear tetrahedral finite elements to cope with large deformations and rotations (Nesme et al., 2005). The simulation time is scaled such that the simulated MV closure is ten times longer than what is observed in the images (from 70 ms to 150 ms) to handle the strong and discontinuous contact forces, as in (Votta et al., 2008). An implicit Euler solver is used to update mesh positions (Baraff and Witkin, 1998). We finally stress that the pipeline is completely integrated, from model estimation to simulation, although the user can manually adjust the models if necessary.

3. Experiments and results

Three experiments were carried out. We first evaluated the accuracy of the anatomical model estimation. We then performed a sensitivity analysis of our biomechanical model, followed by a systematic evaluation on 25 consecutive subjects. We finally applied our framework to predict MitralClip intervention in one case for whom postoperative data was available.

3.1. Validation of the MV anatomical model

The performance of the automatic estimation of the MV apparatus was evaluated on 200 3D+t TEE images from 120 patients with a wide range of diseases (MV prolapse, calcified mitral annulus, stenosis, ventricular dysfunction, etc.). Images were acquired with different angulation, field of view and resolution (spatial and temporal). Threefold cross-validation against manual delineation yielded an average point-to-mesh error of 2.75 ± 0.86 mm. Qualitative evaluation showed that the MV was faithfully tracked throughout the cardiac sequence, even during valve closure and opening when the dynamics are fast (Fig. 9). Computation time was 4.8 s per 3D volume (Intel Core2Duo, 2.66 GHz quad core, 2 GB RAM). A thorough evaluation of model estimation is beyond

the scope of this study, more comprehensive evaluations can be found in (Ionasec et al., 2010; Grbić et al., 2010; Voigt et al., 2011b).

3.2. Evaluation of MV closure simulation

3.2.1. FEM convergence analysis

We first determined the spatial resolution and the time step that are required for computationally efficient and accurate simulations. To this end, we quantified the numerical convergence of the dynamic system by computing the difference between the simulation results at a given spatial/temporal resolution and the result obtained at the finest discretization. Sub-millimetric errors were considered as satisfactory, compared to image resolution (between 0.75–1.58 mm). The analyses were performed using the MV anatomy and boundary conditions of Patient 1. The parameters reported in Table 1 were used. The rest lengths of marginal and basal chordae estimated from the images were increased by 30% and 10% respectively to better capture the observed MV closure (see Section 3.2.3 and Fig. 17 for details and simulation accuracy with respect to the ground truth).

3.2.1.1. Spatial convergence analysis.
We first fixed the radial resolution $v_{res} = 30$ (Section 2.2) and simulated MV closure with the circumferential resolutions $u_{res} = 30, 40, 50$, corresponding respectively to 9408, 12,768, 16,128 elements with 1.67 mm, 1.24 mm and 0.98 mm average edge-length. As one can see from Fig. 10, u_{res} had sub-millimetric effects on the results, as confirmed by the point-to-mesh distance with respect to the result obtained with the finest mesh, i.e. $u_{res} = 50$ ($e_{u_{res}=30} = 0.48 \pm 0.28$ mm, $e_{u_{res}=40} = 0.46 \pm 0.25$). We then fixed $u_{res} = 30$ and used $v_{res} = 10, 20, 30$, corresponding respectively to 2688, 6048 and 9408 elements with 4.89 mm, 2.49 mm and 1.67 mm average edge-length. As it can be seen in Fig. 11, the simulation at $v_{res} = 10$ was significantly different from the others (point-to-mesh distance with the result obtained with $v_{res} = 30$: $e_{v_{res}=10} = 0.74 \pm 0.85$ mm). In particular, the PL position was different. Results at $v_{res} = 20$ and $v_{res} = 30$ were closer to each other ($e_{v_{res}=20} = 0.31 \pm 0.23$ mm), suggesting numerical convergence at $v_{res} = 30$. Those results also hold for non-reported simulations at higher v_{res} and u_{res}. Therefore, meshes generated with $u_{res} = v_{res} = 30$ (9408 elements, 1.67 mm average edge-length) were used for all subsequent simulations.

3.2.1.2. Temporal convergence analysis.
Although Euler implicit scheme theoretically allows large time steps dt, collision detection can be hampered if dt is too large, when displacement amplitude can be larger than collision alarm distance d_c (Section 2.3.3). We investigated the effects of time discretization on the simulations by computing MV closure with $dt = 10^{-1}$ s, 10^{-2} s, 10^{-3} s and 10^{-4} s. Fig. 12 reports the point-to-point distances between the closed MV computed with $dt = 10^{-1}$ s, 10^{-2} s and 10^{-3} s and the closed MV computed with $dt = 10^{-4}$ s. Numerical convergence

---

[1] http://www.sofa-framework.org.
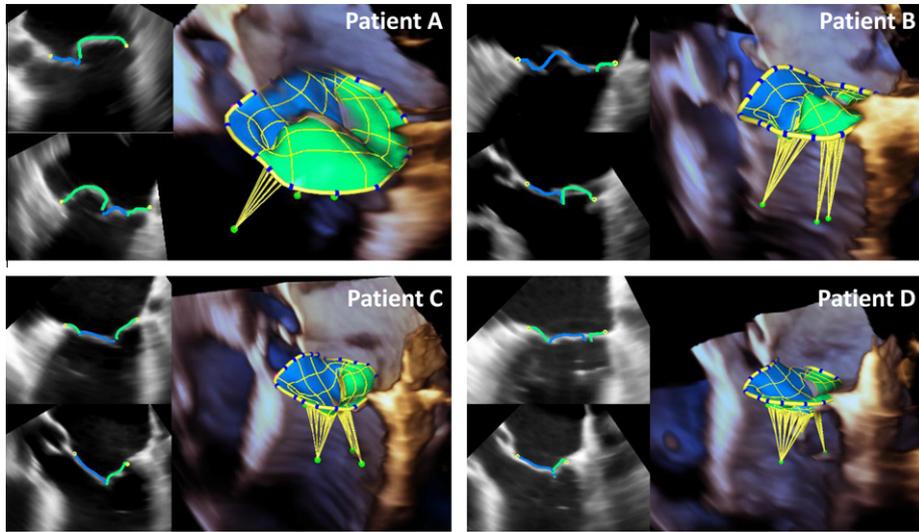
Fig. 9. Automatic detection of the MV apparatus on 3D+t TEE sequences of four patients with different diseases. The model accurately fits patients' MV in the images.
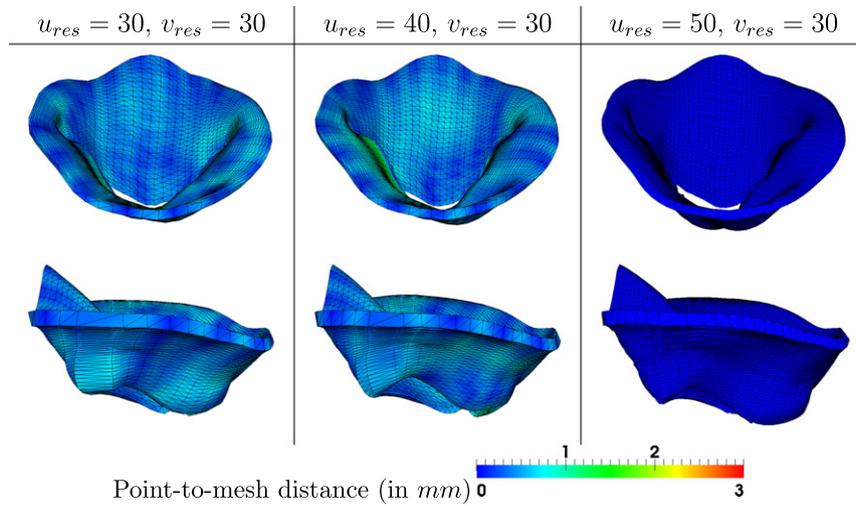
Fig. 10. Effect of the circumferential resolution u_{res} on the simulation. Only millimetric differences were visible. Colors encode point-to-mesh distance computed with respect to the solution obtained at $u_{res} = 50$, $v_{res} = 30$. (For interpretation of the references to colour in this figure legend, the reader is referred to the web version of this article.)
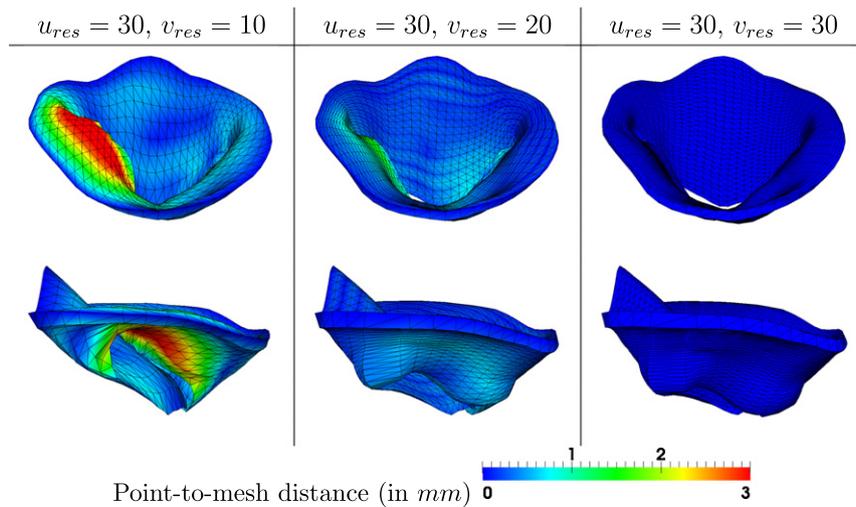
Fig. 11. Effect of the radial resolution v_{res} on the simulation. At $v_{res} = 10$, MV closure simulation yielded a totally different result (see posterior leaflet), while convergence can be seen for $v_{res} \geqslant 20$.
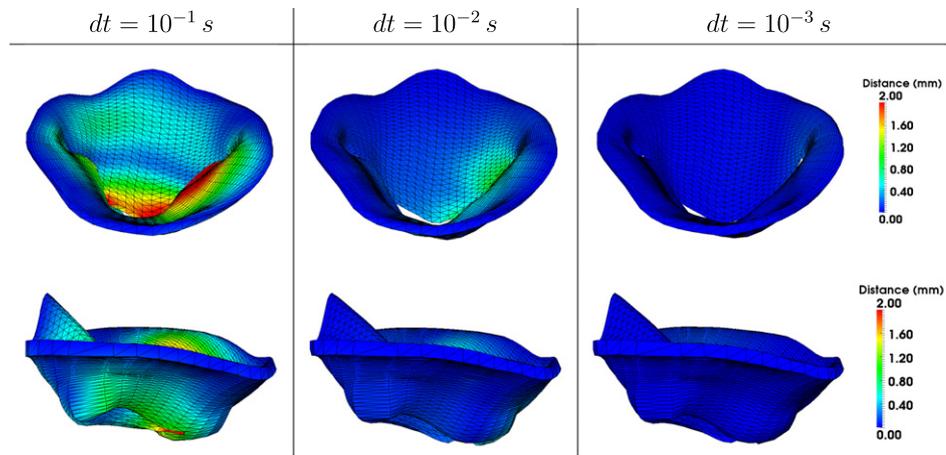
Fig. 12. Effect of the time step dt on the simulation. Colors encode point-to-point distance computed with the result obtained at $dt = 10^{-4}$ s. Convergence was achieved at $dt = 10^{-3}$ s but $dt = 10^{-2}$ s already yielded voxel accuracy. (For interpretation of the references to colour in this figure legend, the reader is referred to the web version of this article.)

was clearly reached at $dt = 10^{-3}$ s (mean error: 0.03 ± 0.04 mm, max.: 0.21 mm). $dt = 10^{-2}$ s yielded already voxel accuracy (mean error: 0.20 ± 0.20 mm, max.: 1.84 mm) but $dt = 0.1$ s was too large (mean error: 0.62 ± 0.61 mm, max.: 3.50 mm). With that time step, inter-leaflet collisions were not detected due to the large displacements, and both leaflets interpenetrated (red zone in Fig. 12). $dt = 10^{-2}$ s seemed to be a good compromise between accuracy and computational efficiency.

3.2.2. Sensitivity analysis of biomechanical model parameters

We analyzed the sensitivity of our framework with respect to boundary conditions and chordae configuration since these parameters were reported to influence significantly FEM (Stevanella et al., 2009) and mass-spring (Hammer et al., 2011) simulations. We used the same parameters as in the previous section, with $u_{res} = v_{res} = 30$ and $dt = 0.01$ s.

3.2.2.1. Sensitivity to boundary conditions.
We evaluated the effects of boundary conditions on the computed MV closure by succes-

sively disabling mitral annulus motion, papillary tips motion and both (Fig. 13). When the mitral annulus was fixed, the MV did not close anymore, with a significant regurgitant hole. When the papillary tips were fixed, the AL belly excessively billowed into the atrium. This experiment further confirms the importance of patient-specific boundary conditions, as previously suggested by (Stevanella et al., 2009) based on stress/strain analyses.

3.2.2.2. Sensitivity to marginal chordae properties.
Chordae distribution can vary from patient to patient (Kunzelman and Cochran, 1990). We thus investigated the impact of the number of marginal chordae on the simulation by computing MV closure with 56, 28, 20, 16 and 12 marginal chordae evenly attached to the free edges. All other parameters were kept constant (Table 1). MV dynamics are quantified by computing the distance between the leaflet tips and the annulus plane, which was defined by the two trigones and the posterior annulus mid-point (Fig. 3). Not surprisingly, varying the number of marginal chordae modified leaflets dynamics (Fig. 14). For instance, AL free edge came closer to the mitral
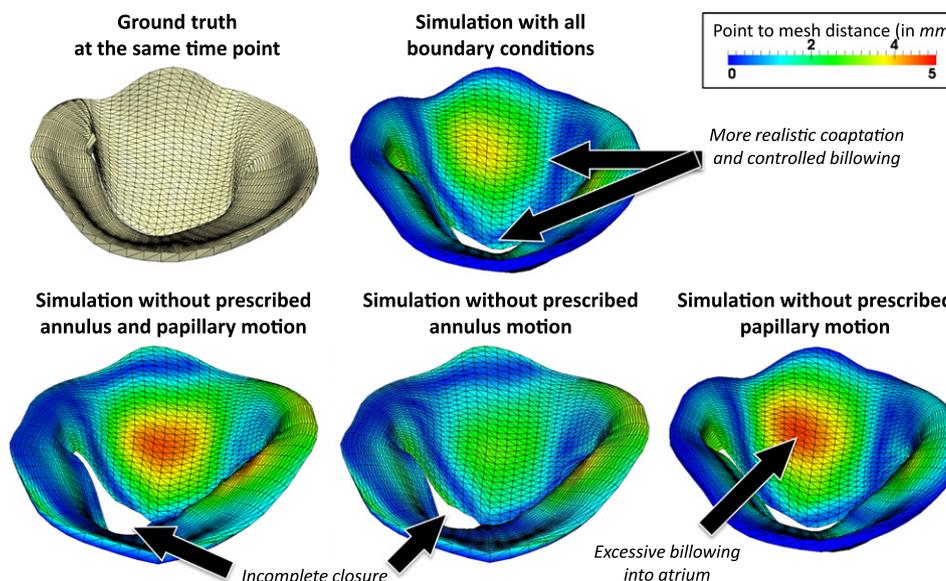
Fig. 13. Effect of boundary conditions on the simulation. Simulations without any of the boundary conditions was significantly less accurate. Mitral annulus motion favored leaflet coaptation while papillary motion helped control anterior leaflet billowing. Distance measured with respect to ground truth.

Anterior tip to mitral annulus plane distance (in mm)
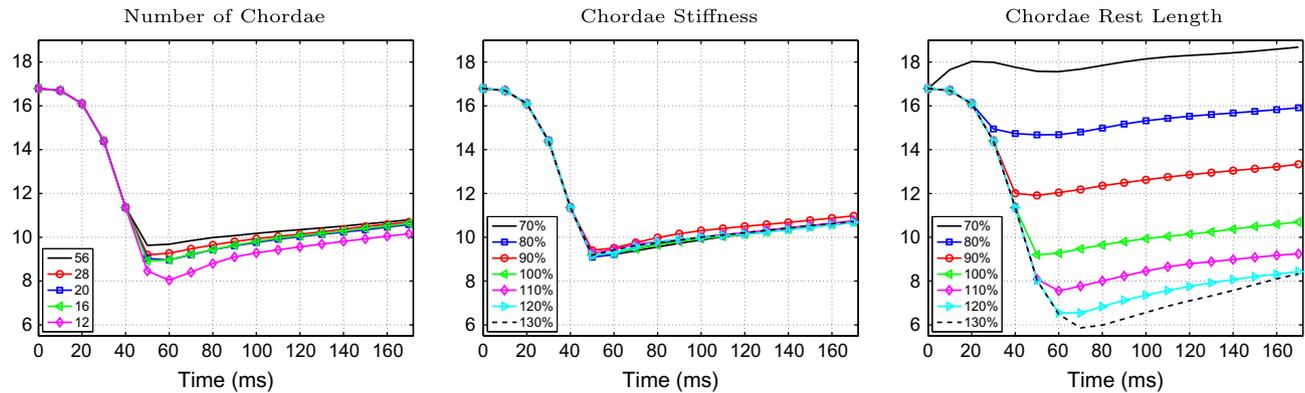
Posterior tip to mitral annulus plane distance (in mm)
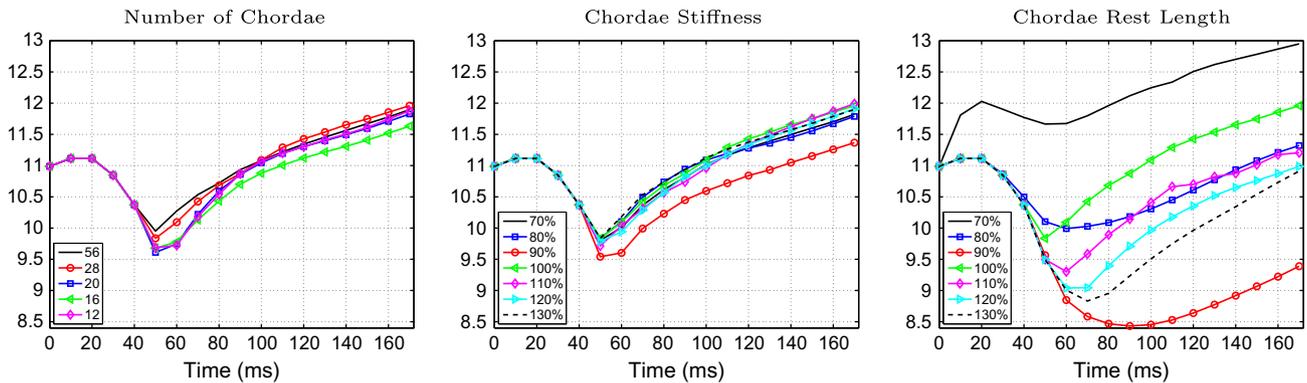
Fig. 14. Effect of chordae parameters on the simulation. Chordae rest length had a significant influence on MV dynamics, compared to the number of marginal chordae and chordae stiffness. Chordae rest length can also alter MV dynamics by modifying inter-leaflet collisions (pink curve, right panels). (For interpretation of the references to colour in this figure legend, the reader is referred to the web version of this article.)

annulus as the number of chordae decreased, since the leaflet is less taut. This feature was also visible for the PL, although less evident due to smaller tip motion. As the maximum difference in tip displacement was ⩽1.65 mm for the anterior tip and ⩽0.64 mm for the posterior tip, we preferred to use 28 marginal chordae to be consistent with previous studies (Stevanella et al., 2011b). It should be noted though that local MV dynamics can be modified if chordae distribution is locally changed, to model chordae rupture for instance.

We evaluated the sensitivity of the simulation with respect to chordae stiffness. MV closure was computed with stiffnesses varying from −30% to +30% of the standard values (Fig. 14, mid panel). We used 28 marginal chordae for that experiment. Interestingly, the variations were similar both in trends and amplitude to those obtained in the previous experiment (maximum difference in tip displacement ⩽0.44 mm for the anterior tip, ⩽0.46 mm for the posterior tip). This can be explained by the law of parallel springs, since chordae were always evenly distributed.

In both experiments, all configurations yielded identical results at $t < 40$ ms. During that time interval, all chordae were under compression (no tension), as papillaries and leaflet free edges were moving synchronously. Leaflets were thus free to move. Differences appeared only later, when chordae started to tense and control leaflets motion.

Chordae rest length $L_{i,0}$ (Section 2.3.2) was also reported to have a significant influence on MV dynamics (Hammer et al., 2011). In our framework, $L_{i,0}$ is the distance between papillary tips and insertion points at end diastole. Computing MV closure with $L_{i,0} \pm 10\%$, 20% and 30% yielded significant differences in simulation results

(Fig. 14, right panels). By changing the rest length from −30% to +30%, differences in tip motion amplitude of 10.03 mm for the anterior tip and 3.87 mm for the posterior tip were observed. When the rest length was too long, the leaflets were free to fold and the tips eventually attained the mitral annulus plane. When the rest length was too short, the leaflets did not close at all. It is therefore crucial to set up this parameter accordingly for each patient for accurate simulations.

Based on these results, a three-step personalization strategy can be derived. First, insertion points distribution is assessed such that

Table 2
Point-to-mesh distances between simulation and ground truth. Values reported as mean ± SD (95th-percentile). The average error (1.49 ± 0.62 mm) was of the same order of magnitude as that of the automatic detection (2.75 ± 0.86 mm). ☆, ◇ and □ denote satisfactory, passable and unsatisfactory simulations.

Patient	Point-to-mesh error (mm)	Patient	Point-to-mesh error (mm)
01	1.67 ± 1.50 (4.92), □	14	2.01 ± 1.81 (5.78), ◇
02	1.46 ± 2.09 (6.23), □	15	1.41 ± 1.09 (3.61), □
03	3.04 ± 2.56 (8.19), □	16	1.38 ± 1.04 (3.54), ◇
04	3.14 ± 2.91 (8.77), □	17	1.70 ± 1.64 (4.73), ◇
05	1.34 ± 1.43 (4.29), ◇	18	1.28 ± 1.14 (3.83), ◇
06	1.21 ± 1.14 (3.78), ◇	19	1.07 ± 0.91 (2.95), □
07	0.61 ± 0.52 (1.58), ☆	20	0.90 ± 0.72 (2.32), ☆
08	0.99 ± 0.71 (2.49), ☆	21	1.44 ± 1.57 (4.79), ◇
09	1.19 ± 1.00 (3.20), □	22	2.43 ± 2.03 (6.31), □
10	1.43 ± 1.33 (4.05), ☆	23	0.94 ± 0.87 (2.80), ◇
11	1.83 ± 2.96 (9.14), □	24	0.79 ± 0.84 (2.61), ☆
12	1.07 ± 0.84 (2.61), ☆	25	1.14 ± 1.31 (4.38), ◇
13	1.66 ± 1.68 (5.23), ☆		

the main features of the closed valves are captured. This can be achieved by starting with a homogeneous distribution and then removing chordae apparently ruptured. The insertion points are then fixed and the rest length estimated individually such that the position of the free edges matches what is observed in the images. Finally chordae stiffnesses are adjusted to further refine the simulation results. The process is iterated until convergence.

3.2.3. Biomechanical model generalization with respect to tissue properties

Our integrated framework enabled us to evaluate the generalization of the biomechanical model in terms of tissue parameters on 25 consecutive patients. The objective was to assess how well MV closure can be captured using patient-specific anatomy and boundary conditions only, tissue properties being set according to Table 1.

3.2.3.1. Patient selection and experimental protocol. 25 patients were randomly selected from five hospitals, representing a large spec-trum of heart diseases (MV diseases, aortic valve diseases, myocardium infarction, etc.). For these patients, standard 3D+t TEE images of the MV were acquired (image resolution: 0.75–1.58 mm isotropic, number of frames: 7–28 (median: 14), covering the full cardiac cycle). MV closure was visible during two to four frames (average duration: 0.197 s). The dynamic models of MV anatomy were automatically estimated on all time frames of the sequences. To minimize bias in the evaluation of the simulation, an expert (M.H.) carefully verified the estimated models. When errors were visible, the expert could interactively manipulate the landmarks and leaflet surfaces in user-friendly 2D views, the shape constraint and temporal model ensuring anatomical and temporal consistency automatically (Ionasec et al., 2010). In particular, papillary tips were carefully verified using all temporal information. The resulting models were then used as *ground truth*.

The anatomical model at the time frame just before closure, which corresponds to the end-diastole time point, was used to simulate MV closure. Boundary conditions were estimated from the images. The pressure profile described in Section 2.3.3 was applied

Point-to-mesh distance to ground truth (in mm)
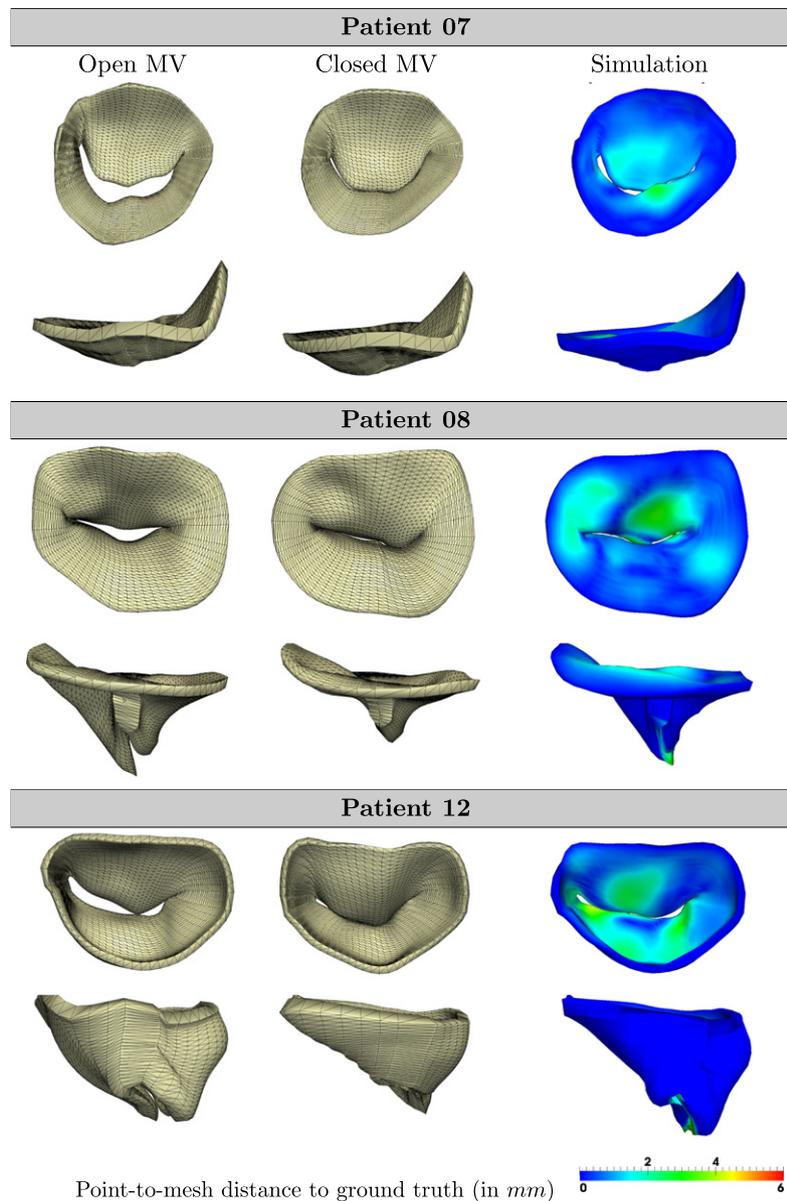
Fig. 15. Simulated MV closure in three patients compared to observed MV shape. These cases were visually ranked as satisfactory.
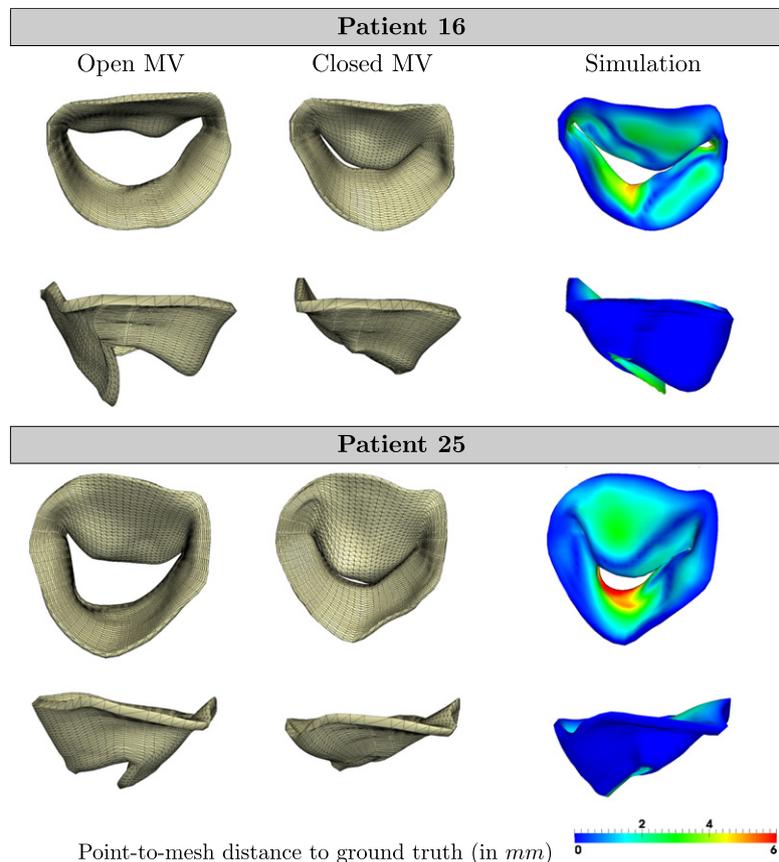
Fig. 16. Simulated MV closure in two patients compared to observed MV shape. Partial MV closure was achieved in these cases, mainly because of an incomplete closure of posterior leaflet.

and simulation was scaled as described in Section 2.5. The simulated closed valve was compared to the ground truth estimated at the first time frame at which the MV was observed closed.

3.2.3.2. MV closure simulation. Table 2 reports the average point-to-mesh distances from the simulations to the ground truth for every patient. Population-wise, the average error was 1.49 ± 0.62 mm, which was of the same order of magnitude of the automated detection and in the range of values reported in the literature (Burlina et al., 2010; Hammer et al., 2011; Sprouse et al., 2011). We qualitatively evaluated the results by ranking them as *satisfactory* if the closure observed in the images was captured (Fig. 15), *passable* if closure was only partial (Fig. 16), or *unsatisfactory* if the valve was still open or not corresponding to the observation (Fig. 17). With those criteria, simulations were qualified as satisfactory in seven patients (28%, average point-to-mesh error: $e_{mean} = 1.07 \pm 0.36$ mm, $e_{max} = 1.66$ mm), passable in nine patients (36%, $e_{mean} = 1.38 \pm 0.31$ mm, $e_{max} = 2.01$ mm) and unsatisfactory in nine patients (36%, $e_{mean} = 1.91 \pm 0.77$ mm, $e_{max} = 3.13$ mm).

The biomechanical model was able to capture MV closure in seven patients with an accuracy equivalent to the image resolution. The other cases confirmed that tissue properties required further personalization, in particular in a population of patients where leaflet properties and chordae tendineae configurations can vary significantly among individuals. Large errors were often due to non-optimal chordae rest length, as observed in patient one and 17 for instance (Fig. 17, black arrows). In these two cases, the AL remained open, pulled down by tensed chordae. Although a complete inverse problem analysis of our population is out of the scope of this manuscript, we evaluated the ability of our model to cap-

ture valve closure for those two patients and for one case rated as satisfactory (Patient 10) by manually adjusting chordae rest length based on the full dynamic data. Chordae were grouped per papillary and per type (marginal and basal), yielding four groups. For each group, chordae rest length was multiplied by a factor, which was determined by qualitatively minimizing the differences between the simulation results and the models computed from the images. The number of chordae and their stiffness were fixed to their default values. Fig. 17 shows the results obtained before and after personalization for Patient one and 17. Fig. 18, top row, shows the results for Patient 10. Point-to-mesh errors after personalization are reported in Table 3. As it can be seen from the figures, adjusting chordae rest length significantly improved the accuracy of MV closure prediction. Further improvement could be reached by adjusting all biomechanical parameters at once through inverse problem methods (Powell, 2008).

3.2.3.3. Computation time. Simulation was performed in ≈ 0.3 frames per second on a desktop machine (Intel Xeon, 2.40 GHz octo-core, 4 GB RAM), mono-core execution, which amounts to ≈ 10 min. No particular optimizations were implemented. Simulation profiling showed that about 75% of computational costs were dedicated to collision handling. GPU-based collision methods (Courtecuisse et al., 2011) can therefore significantly speed-up the simulation. The entire process, from the 3D+t TEE images to anatomical model verification to the forward simulation (no personalization), took about 14 min. Chordae rest length personalization was achieved by running several forward simulations in parallel (six simulations at a time). The full process took less than one hour for the three cases reported in Table 3.

Point-to-mesh distance to ground truth (in mm)
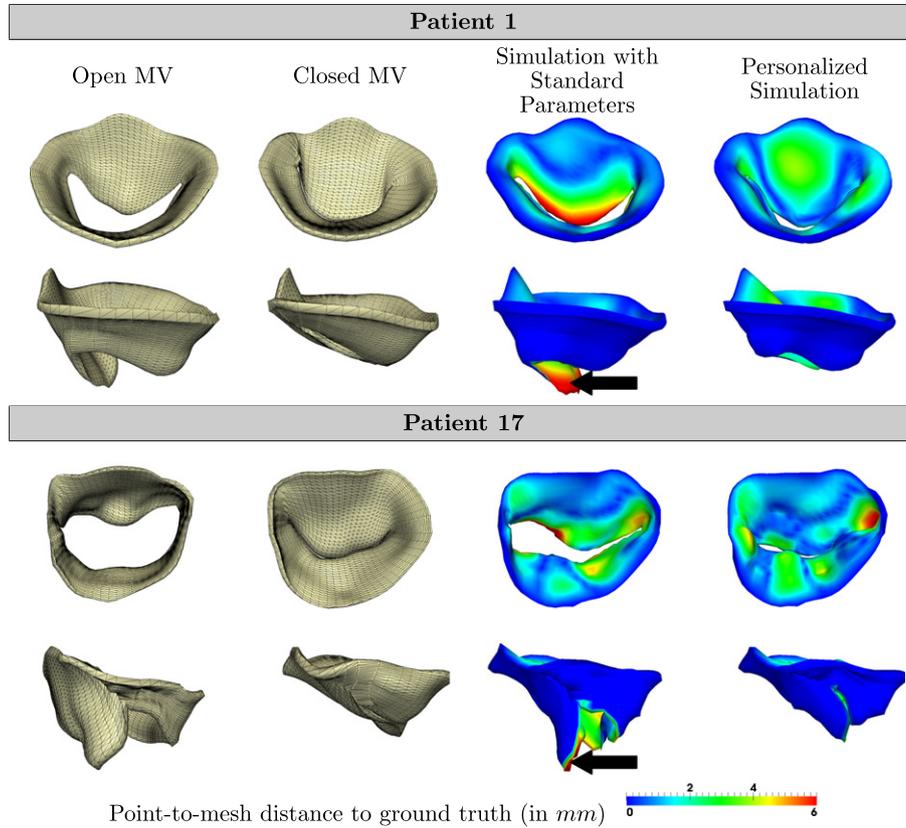
Fig. 17. Simulated MV closure in two patients compared to observed MV shape. Simulation with generic tissue parameters was not able to capture MV closure in these patients. Too short chordae prevented the anterior leaflet to close *(black arrow)*. Adjusting chordae rest length significantly improved the results.
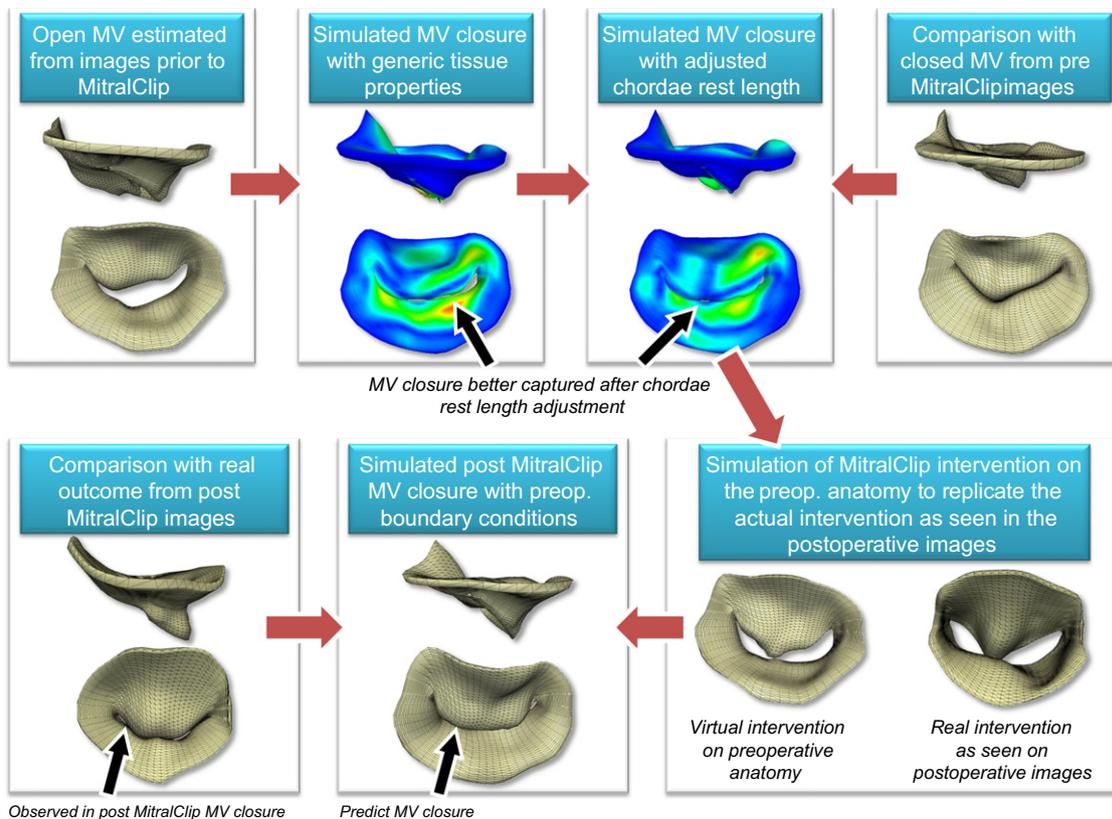
Fig. 18. The prediction power of the biomechanical model was evaluated by simulating MitralClip intervention on the preoperative anatomy of Patient 10 and comparing the result with the real outcome. The result was qualitatively consistent with the true postoperative outcome.

Table 3
Point-to-mesh distance between simulation and ground truth after chordae rest length adjustment in three cases. Values reported as mean ± SD (95th-percentile). Personalizing MV chordae rest length enabled us to better capture MV closure than with standard rest length (Table 2).

Patient	Point-to-mesh error (mm)
01	1.27 ± 0.87 (2.96)
10	1.12 ± 1.10 (3.40)
17	1.50 ± 1.27 (4.25)

3.3. Simulation of MitralClip

As it has been shown in the previous section, it is possible to find a set of parameters that would enable one to simulate the MV closure of a specific patient. Yet, the computational model may still not be able to predict changes in MV physiology after modifications of cardiovascular parameters or therapies. We tested the ability of our framework to predict the outcome of MV intervention based on preoperative data only. Intra-operative 3D+t TEE images of the MV before, during and after MitralClip release were available for Patient 10. We first improved the accuracy of the simulated MV closure before clip release by slightly personalizing chordae rest length (10% higher than the distance between papillary tips and leaflet free edges measured at end diastole) (Table 3). We then simulated the MitralClip intervention on the pre-clip anatomy as described in Section 2.4. The virtual intervention was performed in real-time (2 frames per second). We finally applied the pressure profile on the ventricular surface and the preoperative boundary conditions to predict MV closure just after release of the device. Biomechanical parameters were kept unchanged. Fig. 18 illustrates each step of the experiment. The model was able to simulate MV closure after the intervention with results similar to what was observed in the post-clip images, suggesting promising prediction power. One should remark that the difference in mitral annulus shape between the simulated clipped valve and the real outcome is due to the different boundary conditions. Here, preoperative boundary conditions were applied to reproduce a real-case scenario where therapy outcome is unknown.

4. Discussion and conclusions

4.1. Discussion

In this work, MV anatomy and boundary conditions were estimated from 3D+t TEE images. Our approach can be easily applied to other imaging modalities (Grbić et al., 2010). Although difficult to visualize, papillaries could be detected by our framework as the temporally-consistent detection algorithm was trained on annotations carefully verified by clinicians (Ionasec et al., 2010). Nonetheless, to avoid bias in the evaluation of the simulations, we utilized anatomical models that were verified and corrected by an expert (M.H.) when required. However, that manual interaction, which took about 1–2 min (Stiver et al., 2011), was not a limitation.

Recent *in vivo* studies highlighted the importance of AL shape in MV closure (Stevanella et al., 2011a). No general trend in AL shape could be observed in our population of patients, but the features reported in (Stevanella et al., 2011a) could be identified in some patients, in particular during systole (Fig. 19) (these patterns were more difficult to distinguish during diastole). The AL was more concave towards the atrium near the annulus, and more convex close to the free edges in the septolateral direction. In the commissure-commissure direction, the surface was rather convex towards the atrium at the belly. Comprehensive analysis of that aspect and its consequence on leaflet strain and stress distribution will be the subject of a future study.

Our sensitivity analysis showed that the motion of the mitral annulus and papillary tips significantly contributed to leaflet coaptation and systolic shape. The observed importance of boundary conditions agrees with other published studies on that aspect, as in (Stevanella et al., 2009). Estimating automatically these boundary conditions from the images is therefore a key feature of our framework. We also found that chordae rest length had more impact on MV closure than chordae stiffness. Unfortunately, chordae length cannot be measured from the images directly as they are not visible. We thus approximated that parameter as the distance between papillary tips and leaflet free edges at end diastole. This strategy enabled us to simulate the observed MV coaptation in seven cases. For those patients, the initial, open MV configuration was already close to the closed configuration, and therefore the influence of chordae rest length was less significant. Simulated MV closure of valves widely open was more challenging. Co-rotational elements being able to simulate large deformations accurately, the issue was mainly related to chordae rest length, which were under-estimated by our image-based algorithm, thus preventing the leaflet to close. By increasing the rest length, we managed to capture MV closure in three patients. Inverse problem approaches based on the full MV dynamics can therefore provide more accurate estimations of chordae rest length, although *in vivo* validation would be challenging as chordae are not visible in images.

In that work, the average point-to-mesh distance was used to evaluate simulation accuracy. That metric is commonly used in the literature, thus allowing performance comparison. Overall, our systematic analysis on 25 cases yielded an accuracy of the same order of magnitude as the one of the automatic detection.
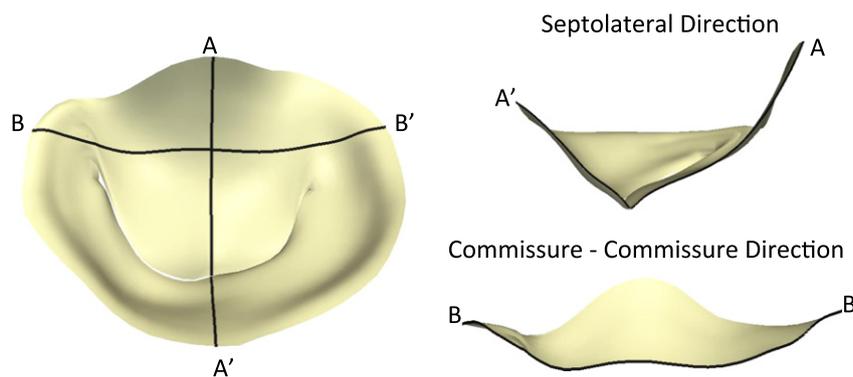
Fig. 19. Mitral valve compound curvature estimated from the images in Patient 1. *See text for details.*

However, visual inspection was still necessary to assess if MV closure was correctly captured. More advanced metrics would thus be necessary when designing cost functions for inverse problem algorithms.

A necessary way to evaluate computational models is to assess their ability to predict therapy outcome. This task is all the more challenging as parameters may not be unique. We thus simulated MitralClip intervention in one patient and compared, with success, model prediction with the real outcome. The virtual intervention was intuitive to perform, our system being fast enough for smooth interactions. Since we were interested in simulating MV closure just after clip release, we considered preoperative data only to mimic a real scenario where postoperative data would not be available. Furthermore, our postoperative data were acquired when the patient was still in the operating room, with catheters and ultrasound probe still in-place, thus minimizing biases in the comparisons. We assumed non-significant tissue remodeling and kept tissue properties unchanged, although the device may have altered tissue integrity locally. Despite these assumptions, obtained results were promising, encouraging further work towards FEM-based therapy planning.

While linear tetrahedra can suffer from locking, and thus underestimate deformations, co-rotational tetrahedra have been designed to cope with large deformations and rotations with good accuracy, as quantified by benchmark tests (Nesme et al., 2005). Visually, the dynamics of our simulations did not show locking nor ghost torques, which appeared when using linear tetrahedra (non-reported experiments). Co-rotational tetrahedra could therefore constitute an alternative to more conventional hexahedra, as tetrahedra meshes are easier to build from complex patient-specific geometries. Quantitative comparisons between the two spatial discretizations are planned for future work.

4.2. Limitations

In this study, MV leaflets were modeled as linear elastic material, whereas biaxial studies showed a strongly non-linear constitutive law (May-Newman and Yin, 1995). Co-rotational tetrahedra were used to cope with large deformations but tissue linearity may yield different tissue stress and strain distributions, which can lead to differences in predicted leaflet position during systole as tissue stretches under external forces. Our framework being modular, computationally efficient methods for hyperelastic materials could be integrated without significant modifications (Marchesseau et al., 2010). Yet, recent studies based on inverse problem suggested that leaflets may have linear behavior *in vivo* (Krishnamurthy et al., 2008; Krishnamurthy et al., 2009), but with Young's moduli higher than those estimated *ex vivo*. Using linear elastic models for *in vivo* simulations may thus be suitable. This study was performed with standard *ex vivo* Young's moduli to be consistent with simulations reported in the literature. Preliminary experiments based on homogeneous *in vivo* Young's moduli, which were extrapolated to human physiology as detailed in (Krishnamurthy et al., 2008) and extrapolated to the PL, resulted in more accurate AL billowing, as already observed in (Skallerud et al., 2011). However, the overall MV had more difficulty to close, in particular the PL due to a stiffer commissure area. Spatially-varying Young's moduli may increase the accuracy of the simulation. Further investigations and experiments on patient-specific anatomies would be necessary to include these new findings into our model.

We modeled leaflets as homogeneous tissues with standard thickness for all patients. It has been shown that leaflets are made up of three layers, with different material properties. Multi-layer models (Prot and Skallerud, 2009) can be beneficial for pathology understanding. However, they introduce additional parameters that may be difficult to estimate from clinical data. Additionally, pathologies can significantly disrupt local tissue properties and leaflet morphology. Modeling these variations will be extremely important to quantify MV biomechanics and predict therapies. Tissue calcification could be quantified from CT imaging for instance, or estimated indirectly from the MV dynamics using inverse problems. Leaflet thickness, which can have significant impact upon MV dynamics, could be estimated from the images. This is possible in CT but more challenging in ultrasound images, which are more prone to noise and artifacts.

Tissue viscosity was neglected as we focused on MV closure during one heart cycle only, as in (Prot et al., 2007; Votta et al., 2008). Yet, published studies on livers reported larger deformations when viscosity is added to hyperelastic models (Marchesseau et al., 2010). Numerical and experimental studies are therefore needed to study the impact of viscosity on leaflet deformations. On the other hand, Rayleigh damping was used in our work to mimic the viscous medium in which the leaflet operates, although its parameters are not physiological. One could use leaflet velocity to estimate Rayleigh coefficients, although the same results could be achieved by modifying blood pressure and chordae stiffness. More detailed models that take into account blood flow dynamics and fluid–structure interaction could thus be more appropriate, offering more control on the modeled system as more physically grounded (Einstein et al., 2010).

A generic pressure profile was used for all simulations. The choice of that profile was motivated by the fact that for all patients, the first frame in which the MV was maximally closed showed an already opened aortic valve. Since pressure traces were not available, we assumed the pressure being already larger than the aortic pressure baseline ($\approx$80 mmHg). Yet, the pressure should be personalized as it can vary from patient to patient. Future experiments will be carried out to adjust that parameter based on MV dynamics and flow information.

Finally, only MV closure was considered in this study, to predict residual regurgitation after therapy. Full cycle simulation may provide insights on the entire MV dynamics and tissue stresses for long-term therapy prognosis. This aspect of MV function will be investigated in future work.

4.3. Perspectives

Our framework opens new technical and clinical avenues. First, the difference between *in vivo* and *ex vivo* leaflet behavior is nowadays believed to be due to an active force that modifies tissue stiffness throughout the cardiac cycle (Krishnamurthy et al., 2009; Stevanella et al., 2011a; Swanson et al., 2011). That mechanism further controls the systolic shape of the AL, which confers a funnel shape on the left ventricle outflow tract and optimize flow motion towards the aorta. Integrating an active component in our biomechanical model will certainly provide further insights into MV physiology (Skallerud et al., 2011). However, additional parameters would be necessary to estimate, which may be challenging using standard clinical data. Furthermore, it is not clear whether explicitly modeling the active force would improve the predictive power of the model, compared to hyperelastic materials or linear elastic models with a time varying stiffness. Numerical studies with subject-specific geometries are necessary to assess that question.

Model personalization is another challenge that needs to be addressed for patient-specific modeling. As demonstrated by the experiments herein, patient-specific geometries and boundary conditions are necessary but not sufficient to simulate MV closure. Tissue properties and chordae anatomy need to be estimated. As our framework is able to estimate dynamic MV models from images, a next step of our study will be to use inverse problem methods to estimate the tissue properties from MV dynamics. Esti-

mating tissue parameters is challenging due to the large parameter space and parameter ambiguity. That is why it is important to use models with few parameters, which are physiologically meaningful and have direct control on the simulation results. Chordae rest length is an example of such a parameter, although its effect can be confused with those of the pressure (which could be solved if one has pressure traces for instance). Similar uniqueness issues arise for leaflet tissue properties, in particular if active stiffening is considered. A solution would be to add more data to constrain the problem, such as dynamics images at different heart rates, flow measurements, etc.

In this study we predicted leaflet closure after MitralClip based on preoperative data. Yet, the intervention can modify heart function as regurgitations are treated. Ventricular systolic pressure could have raised after mitral regurgitation repair as more blood was ejected into the aorta (no data was available), eventually resulting in changes of mitral annulus motion as the myocardium compensates for the increased pressure to preserve ejection fraction. A more detailed model coupling LV and MV (Wenk et al., 2010) may increase prediction accuracy, at the price of additional parameters to adjust. Similarly, it would be interesting to investigate the effects of the device. For instance, tissue properties may have been altered locally by the mechanical clipping. The device may also locally modify fluid patterns, and therefore alter pressure distribution. Numerical studies may provide insights on the effects of the device.

4.4. Conclusions

Translating computational models of MV physiology to clinical practice is a tremendous challenge. Thanks to the high degree of automation, our system enables rapid and interactive simulations of MV function. The user can therefore test therapies *in silico* and assess their outcome. That level of integration will enable one to evaluate the computational models of MV on larger populations, a necessary step before deploying these methods in clinical settings. Our system may thus constitute a first step towards clinical application of MV computational model.

From a research point of view, the proposed framework paves the way to quantitative and systematic evaluation of computational models of the MV. There is growing evidence that patient-specific anatomical models are necessary to fully comprehend MV physiology, in particular in the light of recent *in vivo* studies (Krishnamurthy et al., 2008; Stevanella et al., 2011a). By providing an integrated system for patient-specific modeling, our system may be used as input to more comprehensive inverse problem studies.

In conclusion, we have presented an integrated framework for FEM modeling of MV closure in patients. The level of integration reached by our framework enabled us (i) to perform a sensitivity analysis of MV FEM on patient-specific geometry; (ii) to test the generalization of a biomechanical model in terms of tissue properties in 25 patients, which, to the best of our knowledge, constitutes the largest *in vivo* FEM study reported so far; and (iii) to simulate and predict MitralClip intervention outcome in terms of valve closure in one patient. Our results suggest that FEM models may constitute surrogate tools for mitral valve repair planning.

References

Allard, J., Cotin, S., Faure, F., Bensoussan, P., Poyer, F., Duriez, C., Delingette, H., Grisoni, L., 2007. SOFA – an open source framework for medical simulation. In: Medicine Meets Virtual Reality (MMVR), pp. 13–18.

Avanzini, A., 2008. A computational procedure for prediction of structural effects of edge-to-edge repair on mitral valve. Journal of Biomechanical Engineering 130, 031015.

Avanzini, A., Donzella, G., Libretti, L., 2011. Functional and structural effects of percutaneous edge-to-edge double-orifice repair under cardiac cycle in comparison with suture repair. Proceedings of the Institution of Mechanical Engineers, Part H: Journal of Engineering in Medicine 225, 959–971.

Baraff, D., Witkin, A., 1998. Large steps in cloth simulation. Proceedings of the 25th Annual Conference on Computer Graphics and Interactive Techniques. ACM, pp. 43–54.

Burlina, P., Sprouse, C., DeMenthon, D., Jorstad, A., Juang, R., Contijoch, F., Abraham, T., Yuh, D., McVeigh, E., 2010. Patient-specific modeling and analysis of the mitral valve using 3d-tee. Information Processing in Computer-Assisted Interventions, 135–146.

Chandra, S., Salgo, I., Sugeng, L., Weinert, L., Settlemier, S., Mor-Avi, V., Lang, R., 2011. A three-dimensional insight into the complexity of flow convergence in mitral regurgitation: adjunctive benefit of anatomic regurgitant orifice area. American Journal of Physiology-Heart and Circulatory Physiology 301, H1015–H1024.

Conti, C., Stevanella, M., Maffessanti, F., Trunfio, S., Votta, E., Roghi, A., Parodi, O., Caiani, E., Redaelli, A., 2010. Mitral valve modelling in ischemic patients: finite element analysis from cardiac magnetic resonance imaging. Computers in Cardiology. IEEE, pp. 1059–1062.

Courtecuisse, H., Cotin, S., Allard, J., Soler, L., 2011. Gpu-based interactive simulation of liver resection. ACM SIGGRAPH 2011 Computer Animation Festival. ACM, 98-98.

Einstein, D., Del Pin, F., Jiao, X., Kuprat, A., Carson, J., Kunzelman, K., Cochran, R., Guccione, J., Ratcliffe, M., 2010. Fluid-structure interactions of the mitral valve and left heart: comprehensive strategies, past, present and future. International Journal for Numerical Methods in Biomedical Engineering 26, 348–380.

Feldman, T., Kar, S., Rinaldi, M., Fail, P., Hermiller, J., Smalling, R., Whitlow, P., Gray, W., Low, R., Herrmann, H., et al., 2009. Percutaneous mitral repair with the mitraclip system: safety and midterm durability in the initial everest (endovascular valve edge-to-edge repair study) cohort. Journal of the American College of Cardiology 54, 686–694.

Grashow, J., Yoganathan, A., Sacks, M., 2006. Biaixal stress–stretch behavior of the mitral valve anterior leaflet at physiologic strain rates. Annals of Biomedical Engineering 34, 315–325.

Grbić, S., Ionasec, R., Vitanovski, D., Voigt, I., Wang, Y., Georgescu, B., Navab, N., Comaniciu, D., 2010. Complete valvular heart apparatus model from 4d cardiac ct. Medical Image Computing and Computer-Assisted Intervention–MICCAI 2010. Springer, pp. 218–226.

Hammer, P., del Nido, P., Howe, R., 2011. Anisotropic mass-spring method accurately simulates mitral valve closure from image-based models. Functional Imaging and Modeling of the Heart. Springer, pp. 233–240.

Hammer, P., Vasilyev, N., Perrin, D., Del Nido, P., Howe, R., 2008. Fast image-based model of mitral valve closure for surgical planning. In: Computational Biomechanics for Medicine (MICCAI'08 Workshop), pp. 15–26.

Hermann, E., Faure, F., Raffin, B., 2008. Ray-traced collision detection for deformable bodies. In: 3rd International Conference on Computer Graphics Theory and Applications, GRAPP 2008.

Herrmann, H., Feldman, T., 2006. Percutaneous mitral valve edge-to-edge repair with the evalve mitraclip system: rationale and phase i results. EuroIntervention 1, A36–A39.

Ionasec, R., Voigt, I., Georgescu, B., Wang, Y., Houle, H., Vega-Higuera, F., Navab, N., Comaniciu, D., 2010. Patient-specific modeling and quantification of the aortic and mitral valves from 4-D cardiac CT and TEE. IEEE Transactions on Medical Imaging 29, 1636–1651.

Iung, B., Vahanian, A., 2011. Epidemiology of valvular heart disease in the adult. Nature Reviews Cardiology 8, 162–172.

Jassar, A., Brinster, C., Vergnat, M., Robb, J., Eperjesi, T., Pouch, A., Cheung, A., Weiss, S., Acker, M., Gorman III, J., et al., 2011. Quantitative mitral valve modeling using real-time three-dimensional echocardiography: technique and repeatability. The Annals of Thoracic Surgery 91, 165–171.

Krishnamurthy, G., Ennis, D., Itoh, A., Bothe, W., Swanson, J., Karlsson, M., Kuhl, E., Miller, D., Ingels Jr, N., 2008. Material properties of the ovine mitral valve anterior leaflet in vivo from inverse finite element analysis. American Journal of Physiology-Heart and Circulatory Physiology 295, H1141–H1149.

Krishnamurthy, G., Itoh, A., Bothe, W., Swanson, J., Kuhl, E., Karlsson, M., Craig Miller, D., Ingels, N., 2009. Stress–strain behavior of mitral valve leaflets in the beating ovine heart. Journal of Biomechanics 42, 1909–1916.

Kunzelman, K., Cochran, K., 1990. Mechanical properties of basal and marginal mitral valve chordae tendineae. ASAIO Journal 36, M405.

Kunzelman, K., Cochran, R., Chuong, C., Ring, W., Verrier, E., Eberhart, R., 1993. Finite element analysis of the mitral valve. The Journal of Heart Valve Disease 2, 326.

Kunzelman, K., Einstein, D., Cochran, R., 2007. Fluid–structure interaction models of the mitral valve: function in normal and pathological states. Philosophical Transactions of the Royal Society B: Biological Sciences 362, 1393.

Lau, K., Diaz, V., Scambler, P., Burriesci, G., 2010. Mitral valve dynamics in structural and fluid-structure interaction models. Medical Engineering & Physics 32, 1057–1064.

Lau, K., Díaz-Zuccarini, V., Scambler, P., Burriesci, G., 2011. Fluid–structure interaction study of the edge-to-edge repair technique on the mitral valve. Journal of Biomechanics 44, 2409–2417.

Maisano, F., Torracca, L., Oppizzi, M., Stefano, P., d'Addario, G., La Canna, G., Zogno, M., Alfieri, O., 1998. The edge-to-edge technique: a simplified method to correct mitral insufficiency. European Journal of Cardio-thoracic Surgery 13, 240.

Mansi, T., Voigt, I., Mengue, E., Ionasec, R., Georgescu, B., Noack, T., Seeburger, J., Comaniciu, D., 2011. Towards patient-specific finite-element simulation of

MitralClip procedure. Medical Image Computing and Computer-Assisted Intervention–MICCAI 2011. Springer, pp. 452–459.

Marchesseau, S., Heimann, T., Chatelin, S., Willinger, R., Delingette, H., 2010. Fast porous visco-hyperelastic soft tissue model for surgery simulation: application to liver surgery. Progress in Biophysics and Molecular Biology 103, 185–196.

May-Newman, K., Yin, F., 1995. Biaxial mechanical behavior of excised porcine mitral valve leaflets. American Journal of Physiology – Heart and Circulatory Physiology 269, H1319–H1327.

May-Newman, K., Yin, F., 1998. A constitutive law for mitral valve tissue. Journal of Biomechanical Engineering 120, 38.

Nesme, M., Payan, Y., Faure, F., 2005. Efficient, physically plausible finite elements. Eurographics (short papers), pp. 77–80.

Powell, M., 2008. Developments of newuoa for minimization without derivatives. IMA Journal of Numerical Analysis 28, 649–664.

Prot, V., Haaverstad, R., Skallerud, B., 2009. Finite element analysis of the mitral apparatus: annulus shape effect and chordal force distribution. Biomechanics and Modeling in Mechanobiology 8, 43–55.

Prot, V., Skallerud, B., 2009. Nonlinear solid finite element analysis of mitral valves with heterogeneous leaflet layers. Computational Mechanics 43, 353–368.

Prot, V., Skallerud, B., Holzapfel, G., 2007. Transversely isotropic membrane shells with application to mitral valve mechanics: constitutive modelling and finite element implementation. International Journal for Numerical Methods in Engineering 71, 987–1008.

Prot, V., Skallerud, B., Sommer, G., Holzapfel, G., 2010. On modelling and analysis of healthy and pathological human mitral valves: two case studies. Journal of the Mechanical Behavior of Biomedical Materials 3, 167–177.

Roger, V., Go, A., Lloyd-Jones, D., Adams, R., Berry, J., Brown, T., Carnethon, M., Dai, S., de Simone, G., Ford, E., et al., 2011. Heart disease and stroke statistics—2011 update: a report from the american heart association. Circulation 123, e18–e209.

Sacks, M., David Merryman, W., Schmidt, D., 2009. On the biomechanics of heart valve function. Journal of Biomechanics 42, 1804–1824.

Schievano, S., Kunzelman, K., Nicosia, M., Cochran, R., Einstein, D., Khambadkone, S., Bonhoeffer, P., 2009. Percutaneous mitral valve dilatation: single balloon versus double balloon. a finite element study. Journal of Heart Valve Disease 18, 28–34.

Schneider, R., Burke, W., Marx, G., del Nido, P., Howe, R., 2011a. Modeling mitral valve leaflets from three-dimensional ultrasound. Functional Imaging and Modeling of the Heart–FIMH 2011. Springer, pp. 215–222.

Schneider, R., Perrin, D., Vasilyev, N., Marx, G., del Nido, P., Howe, R., 2011. Mitral annulus segmentation from four-dimensional ultrasound using a valve state predictor and constrained optical flow. Medical Image Analysis.

Schneider, R., Perrin, D., Vasilyev, N., Marx, G., del Nido, P., Howe, R., 2011. Real-time image-based rigid registration of three-dimensional ultrasound. Medical Image Analysis.

Schneider, R., Tenenholtz, N., Perrin, D., Marx, G., del Nido, P., Howe, R., 2011d. Patient-specific mitral leaflet segmentation from 4D ultrasound. Medical Image Computing and Computer-Assisted Intervention–MICCAI 2011. Springer, pp. 520–527.

Skallerud, B., Prot, V., Nordrum, I.S., 2011. Modeling active muscle contraction in mitral valve leaflets during systole: a first approach. Biomechanics and Modeling in Mechanobiology 10, 11–26.

Sprouse, C., DeMenthon, D., Gammie, J., Burlina, P., 2011. Patient-specific modeling of stress/strain for surgical planning and guidance. In: Engineering in Medicine and Biology Society, EMBC 2011. IEEE, pp. 4309–4313.

Sprouse, C., Yuh, D., Abraham, T., Burlina, P., 2009. Computational hemodynamic modeling based on transesophageal echocardiographic imaging. In: Annual International Conference of the IEEE Engineering in Medicine and Biology Society, 2009 (EMBC 2009). IEEE, pp. 3649–3652.

Stevanella, M., Krishnamurthy, G., Votta, E., Swanson, J., Redaelli, A., Ingels, N., 2011a. Mitral leaflet modeling: importance of in vivo shape and material properties. Journal of Biomechanics 44, 2229–2235.

Stevanella, M., Maffessanti, F., Conti, C., Votta, E., Arnoldi, A., Lombardi, M., Parodi, O., Caiani, E., Redaelli, A., 2011b. Mitral valve patient-specific finite element modeling from cardiac mri: application to an annuloplasty procedure. Cardiovascular Engineering and Technology 1–11. http://dx.doi.org/10.1007/s13239-010-0032-4.

Stevanella, M., Votta, E., Redaelli, A., 2009. Mitral valve finite element modeling: Implications of tissues nonlinear response and annular motion. Journal of Biomechanical Engineering 131, 121010.

Stiver, K., Calleja, A., Ionasec, R., Voigt, I., Thavendiranathan, P., Liu, S., Houle, H., De Michelis, N., Ryan, T., Vannan, M., 2011. Superior reproducibility of automated 3-d surgical anatomy of normal and abnormal mitral valve when compared to a manual approach. In: American Society of Echocardiography.

Swanson, J., Krishnamurthy, G., Kvitting, J., Miller, D., Ingels Jr, N., 2011. Electromechanical coupling between the atria and mitral valve. American Journal of Physiology-Heart and Circulatory Physiology 300, H1267–H1273.

Voigt, I., Mansi, T., Ionasec, R., Mengue, E., Houle, H., Georgescu, B., Hornegger, J., Comaniciu, D., 2011a. Robust physically-constrained modeling of the mitral valve and subvalvular apparatus. Medical Image Computing and Computer-Assisted Intervention–MICCAI 2011. Springer, pp. 504–511.

Voigt, I., Mansi, T., Mihalef, V., Ionasec, R., Calleja, A., Mengue, E., Sharma, P., Houle, H., Georgescu, B., Hornegger, J., et al., 2011b. Patient-specific model of left heart anatomy, dynamics and hemodynamics from 4d tee: a first validation study. Functional Imaging and Modeling of the Heart–FIMH 2011. Springer, pp. 341–349.

Votta, E., Caiani, E., Veronesi, F., Soncini, M., Montevecchi, F., Redaelli, A., 2008. Mitral valve finite-element modelling from ultrasound data: a pilot study for a new approach to understand mitral function and clinical scenarios. Philosophical Transactions of the Royal Society A: Mathematical, Physical and Engineering Sciences 366, 3411.

Votta, E., Maisano, F., Bolling, S., Alfieri, O., Montevecchi, F., Redaelli, A., 2007. The geoform disease-specific annuloplasty system: a finite element study. The Annals of Thoracic Surgery 84, 92–101.

Votta, E., Maisano, F., Soncini, M., Redaelli, A., Montevecchi, F., Alfieri, O., et al., 2002. 3-d computational analysis of the stress distribution on the leaflets after edge-to-edge repair of mitral regurgitation. The Journal of Heart Valve Disease 11, 810.

Watton, P., Luo, X., Yin, M., Bernacca, G., Wheatley, D., 2008. Effect of ventricle motion on the dynamic behaviour of chorded mitral valves. Journal of Fluids and Structures 24, 58–74.

Wenk, J., Zhang, Z., Cheng, G., Malhotra, D., Acevedo-Bolton, G., Burger, M., Suzuki, T., Saloner, D., Wallace, A., Guccione, J., et al., 2010. First finite element model of the left ventricle with mitral valve: insights into ischemic mitral regurgitation. The Annals of Thoracic Surgery 89, 1546.

Zheng, Y., Barbu, A., Georgescu, B., Scheuering, M., Comaniciu, D., 2008. Four-chamber heart modeling and automatic segmentation for 3-d cardiac ct volumes using marginal space learning and steerable features. IEEE Transactions on Medical Imaging 27, 1668–1681.